Three-dimensional vortex structures in a rotating dipolar Bose–Einstein condensate

Ramavarmaraja Kishor Kumar[1], Thangarasu Sriraman[2], Henrique Fabrelli[1], Paulsamy Muruganandam[2] and Arnaldo Gammal[1]

[1] Instituto de Física, Universidade de São Paulo, 05508-090 São Paulo, Brazil
[2] School of Physics, Bharathidasan University, Palkalaiperur Campus, Tiruchirappalli 620024, Tamilnadu, India

E-mail: gammal@if.usp.br

Abstract

We study three-dimensional vortex lattice structures in purely dipolar Bose–Einstein condensate (BEC). By using the mean-field approximation, we obtain a stability diagram for the vortex states in purely dipolar BECs as a function of harmonic trap aspect ratio (λ) and dipole–dipole interaction strength (D) under rotation. Rotating the condensate within the unstable region leads to collapse while in the stable region furnishes stable vortex lattices of dipolar BECs. We analyse stable vortex lattice structures by solving the three-dimensional time-dependent Gross–Pitaevskii equation in imaginary time. Further, the stability of vortex states is examined by evolution in real-time. We also investigate the distribution of vortices in a fully anisotropic trap by increasing eccentricity of the external trapping potential. We observe the breaking up of the condensate in two parts with an equal number of vortices on each when the trap is sufficiently weak, and the rotation frequency is high.

Keywords: Bose–Einstein condensates, vortices, dipolar interaction

(Some figures may appear in colour only in the online journal)

1. Introduction

Vortices in Bose–Einstein condensates (BECs) of alkali atoms first observed in the laboratory in 1999 [1]. Since then numerous experimental and theoretical studies along this direction were performed [2]. For instance, these studies include bending of vortex lines in a cigar shaped trap, array of orderly aligned lattices in the quantum-Hall regime, Tkachenko oscillations in the lowest Landau level and so on [3, 4]. The rotational properties of BECs of alkali atoms are reviewed in [2, 5]. Several techniques such as rotating the magnetic trap, laser stirring, decay of solitons, imprinting vortices using topological phases, superimposing an oscillating excitation to the trapping potential, and applying artificial magnetic fields [2, 6, 7] were adopted in BEC experiments to nucleate the vortices.

Early experiments and theoretical studies on vortices in BEC mostly focused on alkali Bose gases with local and isotropic interaction. In particular, there are many numerical studies proposed to analyse the stationary state of rotating alkali BECs [8]. However, the experimental realization of Bose–Einstein condensation in chromium (^{52}Cr) [9], dysprosium (^{164}Dy) [10], followed by erbium (^{168}Er) [11] has enlightened new directions in understanding the properties of BEC in dipolar quantum gases. These recent works has revealed new phenomena due to the peculiar competition between isotropic short-range contact interaction (CI) and anisotropic long-range dipole–dipole interaction (DDI). The most significant features of the dipolar BECs are the emergence of biconcave shaped states, the dependence of the stability on the trap geometry, the roton-like dip in the dispersion relation for excitation waves, and the d-wave mode of the collapse [12–15]. The rotational properties of dipolar Bose gases have also been studied theoretically in the mean-field regime [16–21]. These studies revealed that the rotational properties of dipolar BECs are strongly influenced by the harmonic trap aspect ratio, DDI strength, CI strength and relative strengths between DDI and CI [20, 21]. Square and triangular vortex lattice structures have been predicted in dipolar BECs loaded in optical lattice potentials [22]. The

stability of dipolar BEC is strongly dependent on the trap geometry and dipolar interaction strength. So far the regime for the stability has been analysed only for the non-vortex states of dipolar BECs without rotation [23, 24]. Most of the previous studies on vortices in dipolar BECs are based on two-dimensional models only [16–20]. However, it will be more realistic to investigate the stationary vortex structures in full three-dimensions as they are readily comparable with experiments.

In this paper, we study the vortex lattice structures of purely dipolar BEC by considering the full three-dimensional Gross–Pitaevskii (GP) equation. In particular, we analyse the stability regime for vortex state in purely dipolar BECs with respect to both trap aspect ratio and DDI strength. The stability of the vortices is confirmed by numerically evolving the vortex states in real-time. We show stationary vortex lattice structures for different trap aspect ratios within the stable regime. Further, we study the collapse dynamics of biconcave shaped condensate during rotation. We calculate the chemical potential, rms (root-mean-square) radius and angular momentum of condensate as a function of rotation frequency. We estimate the number of vortices using Thomas–Fermi (TF) approximation and compare them with that obtained through numerical simulations. Finally, we notice the breaking of the condensate when the rotating dipolar BEC is in the fully anisotropic trap.

The paper is organized as follows. In section 2, we present the mean-field equation to study a dipolar BEC in a rotating trapping potential. In section 3, we show the stability diagram for states without and with vortices in purely dipolar BECs as a function of harmonic trap aspect ratio and DDI strength. In section 4, we study the stationary vortex structures observed numerically as well TF calculation on some physical parameters during rotation of the condensate. Then we investigate the spatial distribution of vortices in a fully anisotropic trap in section 5. Finally, in section 6, we present a brief summary and conclusions.

2. The mean-field GP equation in rotating frame

The pattern of vortices in the BEC can be studied using the mean field GP equation [2, 25]. At ultra-low temperatures the properties of a dipolar BEC of N atoms, can be described by the mean-field GP equation in rotating frame with the non-local nonlinearity of the form [16, 19]:

$$i\hbar \frac{\partial \phi(\mathbf{r}, t)}{\partial t} = \left[-\frac{\hbar^2}{2m}\nabla^2 + V_{\text{trap}}(\mathbf{r}) + \frac{4\pi\hbar^2 aN}{m}|\phi(\mathbf{r}, t)|^2 \right.$$
$$\left. - \Omega L_z + N \int U_{\text{dd}}(\mathbf{r} - \mathbf{r}')|\phi(\mathbf{r}', t)|^2 d\mathbf{r}' \right] \phi(\mathbf{r}, t),$$
$$\tag{1}$$

where $\int d\mathbf{r}|\phi(\mathbf{r}, t)|^2 = 1$. The trapping potential, V_{trap} is assumed to be fully asymmetric of the form

$$V_{\text{trap}}(\mathbf{r}) = \frac{1}{2}m(\omega_x^2 x^2 + \omega_y^2 y^2 + \omega_z^2 z^2),$$

where ω_x, ω_y and ω_z are the trap frequencies, m is the atom mass, and a is the atomic scattering length. $L_z = -i\hbar (x\partial_y - y\partial_x)$ corresponds to the z-component of the angular momentum due to the rotation of the dipolar BEC about z-axis with rotation frequency Ω.

For magnetic dipoles, the dipolar interaction is given by [26, 27]

$$U_{\text{dd}}(\mathbf{R}) = \frac{\mu_0 \bar{\mu}^2}{4\pi} \frac{1 - 3\cos^2\theta}{|\mathbf{R}|^3} \left(\frac{3\cos^2\varphi - 1}{2} \right), \tag{2}$$

where $\mathbf{R} = \mathbf{r} - \mathbf{r}'$ determines the relative position of dipoles, θ is the angle between $\mathbf{R}$ and the direction of polarization, μ_0 is the permeability of free space, and $\bar{\mu}$ is the dipole moment of the atom. φ is the angle between the orientation of dipoles and z-axis. We consider the polarization of magnetic dipoles along the direction of z-axis as long as $\varphi = 0$.

To compare the contact and dipolar interactions, it is convenient to introduce the length scale $a_{\text{dd}} \equiv \mu_0 \bar{\mu}^2 m/(12\pi\hbar^2)$ [28]. ^{52}Cr has a magnetic dipole moment of $\bar{\mu} = 6\mu_B$ (μ_B is the Bohr magneton) so that $a_{\text{dd}} \simeq 16a_0$, where a_0 is the Bohr radius. The DDI strength is expressed as $D = 3Na_{\text{dd}}$.

Convenient dimensionless parameters can be defined in terms of a reference frequency $\bar{\omega}$ and the corresponding oscillator length $l = \sqrt{\hbar/(m\bar{\omega})}$. Using dimensionless variables $\mathbf{r}' = \mathbf{r}/l$, $\mathbf{R}' = \mathbf{R}/l$, $a' = a/l$, $a'_{\text{dd}} = a_{\text{dd}}/l$, $t' = t\bar{\omega}$, $x' = x/l$, $y' = y/l$, $z' = z/l$, $\Omega' = \Omega/\bar{\omega}$, $\phi' = l^{3/2}\phi$, equation (1) can be rewritten (after dropping the primes from all the variables) as

$$i\frac{\partial \phi(\mathbf{r}, t)}{\partial t} = \left[-\frac{1}{2}\nabla^2 + \frac{1}{2}(\gamma^2 x^2 + \nu^2 y^2 + \lambda^2 z^2) \right.$$
$$+ 4\pi aN|\phi|^2 - \Omega L_z + 3Na_{\text{dd}}$$
$$\left. \times \int V_{\text{dd}}^{3D}(\mathbf{R})|\phi(\mathbf{r}', t)|^2 d\mathbf{r}' \right] \phi(\mathbf{r}, t), \tag{3}$$

with

$$V_{\text{dd}}^{3D}(\mathbf{R}) = \frac{1 - 3\cos^2\theta}{|\mathbf{R}|^3} \left(\frac{3\cos^2\varphi - 1}{2} \right), \tag{4}$$

$\gamma = \omega_x/\bar{\omega}$, $\nu = \omega_y/\bar{\omega}$, $\lambda = \omega_z/\bar{\omega}$. We consider the cylindrically symmetric harmonic trap with $\gamma = \nu$ with $\omega_x = \omega_y = \omega_\rho$ and we use the reference frequency $\bar{\omega}$ as ω_ρ. For the fully anisotropic trap, the reference frequency is taken as the geometric mean, that is, $\bar{\omega} = (\omega_x\omega_y\omega_z)^{1/3}$. From now, we only refer to the dimensionless variables.

We perform the numerical simulations of the 3D GP equation (3) using the split-step Crank–Nicolson method described in [29, 30]. The dipolar integral in equation (3) diverges at a short distance in coordinate space. However, this can be circumvented by evaluating the integral in momentum space [27, 31]. For the parameters we used in this work for the dipolar GP with ($a = 0$), there is no minimizer [32, 33], which means there is no actual ground state. So the states we refer here are in fact lowest local minimum states.

The numerical simulations for the cylindrically symmetric and fully anisotropic traps are carried out with $192 \times 192 \times 192$ and $320 \times 128 \times 128$ grid sizes
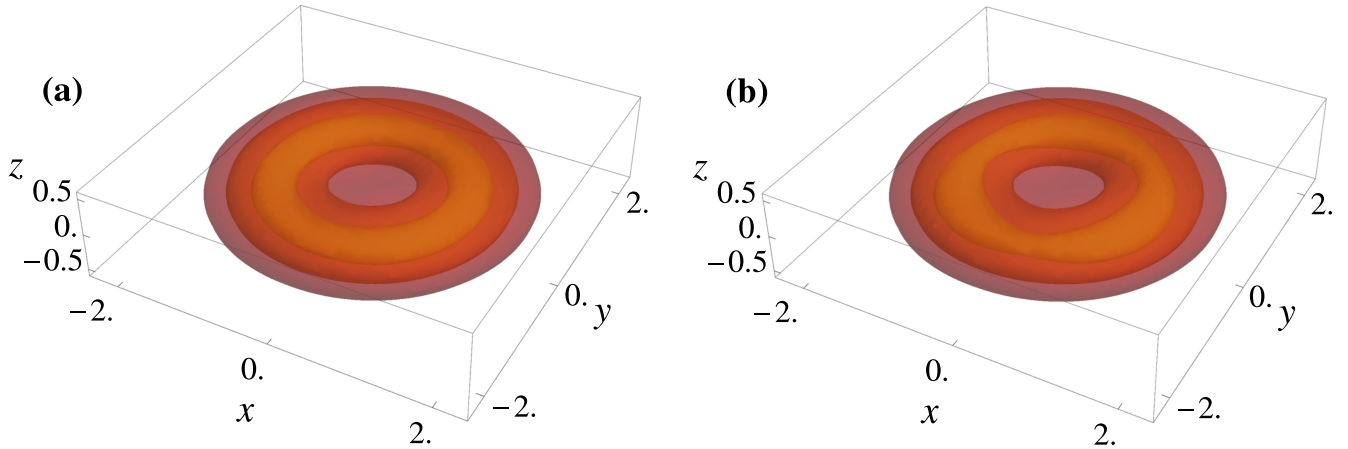
Figure 1. Three-dimensional contour plot showing the transparent view of density oscillation of biconcave shaped condensate for $\lambda = 7$ and $D = 30.4$ in the absence of rotation ($\Omega = 0$) evolve in real-time at time, (a) $t = 0$ and (b) $t = 500$. The contours levels are taken as $|\phi(x, y, z)|^2 = 0.03$ and 0.04.

respectively, with $\Delta x = \Delta y = \Delta z = 0.2$ (space step) and $\Delta t = 0.004$ (time step).

3. Non-vortex and vortex states stability

The important feature of dipolar BEC is the emergence of unusual states. The lowest local minimum state looks like a biconcave shaped structure where the density maximum is not in the center of the condensate [23, 24]. Furthermore, the density oscillations of dipolar BEC with two and four peaks were also reviewed in a fully anisotropic trap. In this section, we are interested in studying the stability and structures in purely dipolar BEC in pancake trap. We have composed the stability diagram for a purely dipolar BEC as a function of the trap aspect ratio (λ) and dipolar interaction strength (D). A similar stability diagram is given in [23]. A dipolar BEC is unstable and collapses for the number of atoms N above a critical value. This can be studied by solving the three-dimensional time-dependent GP equation (3). We have broadened the stability diagram to $\lambda = 30$ and calculated the stability region of the solutions. The biconcave shaped condensate density as shown in figure 1(a) is obtained for the parameters $\lambda = 7$ and $D = 30.4$ from imaginary time propagation. In figure 1(b) we have shown the real-time evolution of the biconcave shaped state. One may note that similar biconcave structures are shown in [23, 24]. Also, we observed such local density fluctuation for the following trap aspect ratios $\lambda = 7, 8, 11, 12, 15, 16, 19,$ and 20. The structured condensates are locally stable in the sense that they are stable only within a local minimum of the energy. Further increase in the number of particles or increase in dipolar interaction energy will change the state to unstable. Here we are interested in rotating this biconcave shaped condensate to study the time evolution. With this objective, we prepared the initial state solution by solving the equation (3) using imaginary time propagation in the absence of rotation ($\Omega = 0$) and then seed the resulting solution in real-time propagation by applying a rotation with frequency $\Omega = 0.5$. At the time of

rotation, the dipoles are immensely pulled towards the outer rim, and two peaks formed as shown in figure 2(b). These two peaks sustain for a very short time, and biconcave shaped condensate becomes unstable.

If we analytically evolve an exact solution with zero angular momentum in the z direction, then term $-\Omega L_z$ in equation (1) plays no role. However, this may not be the case either physically or if it is evolved numerically. Physically, there is always some fluctuation in the wave function field. Fluctuations are random and have in principle contributions of all components of different angular momentum. In the numerical calculations, roundoff errors are always present and give nonzero angular momentum contribution. The term $-\Omega L_z$ will then act on the perturbations, growing them exponentially (modulational instability) and the condensate eventually collapses. The collapse dynamics during rotation is shown as two- and three-dimensional view in figures 2 and 3, respectively. Further, we have constructed a phase diagram illustrating the stability region for stable vortex lattice in $\lambda - D$ parameter space as shown in figure 4. The stable region for vortex lattice is located below the stability region of the states (dashed blue line with empty circles) in figure 4. To carry out this observation, we have prepared the solution using imaginary time propagation with $\Omega = 0$ and progress the solution in imaginary-time with rotation frequency $\Omega = 0.7$. Nevertheless, the stability diagram has been checked for the rotation frequencies in the range 0.7 and 0.99 and no significant changes in the stability boundary are observed. Also, we examined the stability of stationary vortex lattice solutions by evolving in real-time. In figure 4, the region below the solid red line with empty circles corresponds to stable vortex lattice. The vortex states are not stable in the region between the dashed blue with empty circles and solid red line with empty circles. In the next section, we discuss the feasible vortex structures in the shaded region below the solid red line. For the present study, we mainly consider two different harmonic trap aspect ratios, $\lambda = 10$ and 30, and the dipolar interaction strength is chosen within the vortex lattice region in figure 4.
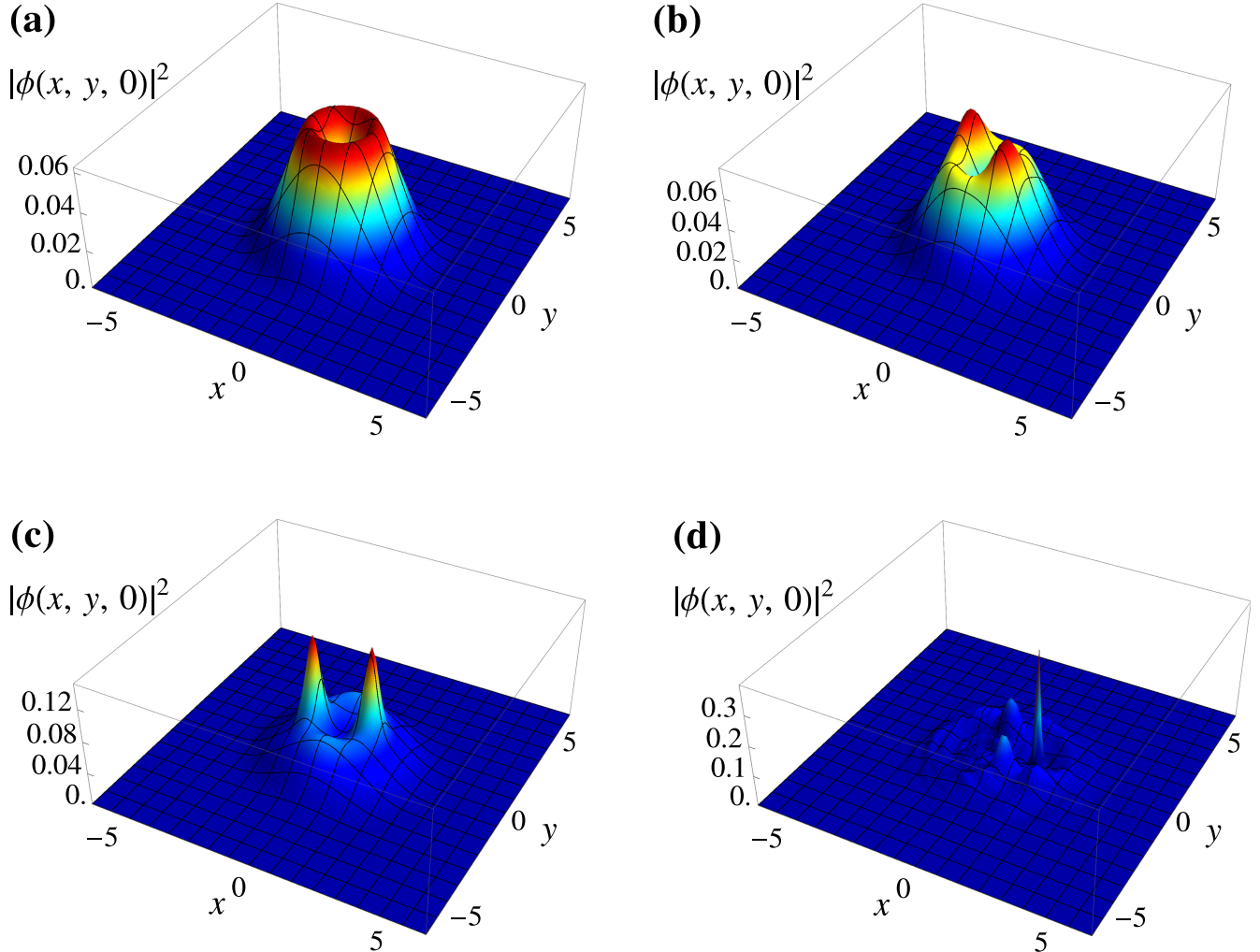
Figure 2. The condensate density $|\phi(x, y, 0)|^2$ for $\lambda = 7$ and $D = 30.4$ in xy plane showing the collapse dynamics of rotating biconcave shaped condensate with $\Omega = 0.5$ in real-time at time, (a) $t = 0$, (b) $t = 60$, (c) $t = 64$, and (d) $t = 65$.
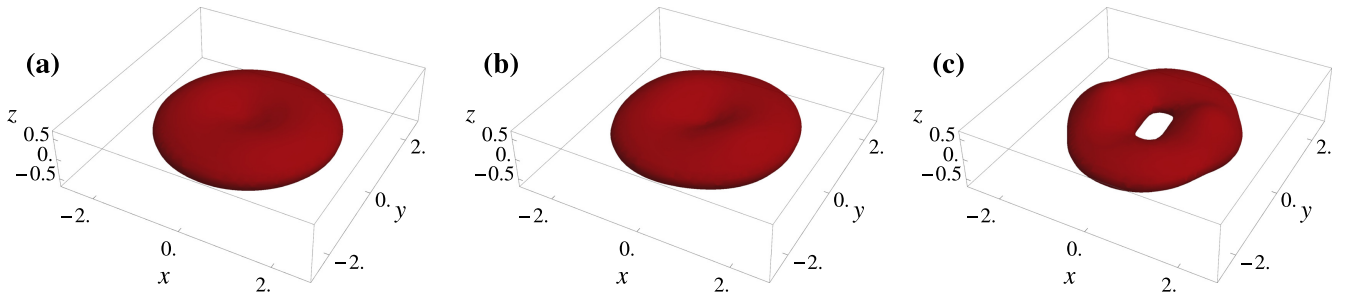

Figure 3. Three-dimensional contour plots of the density $|\phi(x, y, z)|^2$ for $\lambda = 7$ and $D = 30.4$ showing the rotating biconcave shaped condensate with $\Omega = 0.5$ in real-time propagation at times (a) $t = 0$, (b) $t = 60$, and (c) $t = 64$. The contour levels are taken as $|\phi(x, y, z)|^2 = 0.04$.

4. Stationary vortex lattices in purely dipolar BECs

In the following, we show several stationary vortex structures in purely dipolar BEC in the different harmonic trap aspect ratios $\lambda = 10$ and 30, and correspondingly the dipolar interaction strength is chosen as $D \simeq 38$ and 300, respectively. First, in figure 5, we show the stationary vortex structures in $\lambda = 10$. We prepare the initial wave function by solving

equation (3) in the absence of rotation ($\Omega = 0$). The vortices are then created by using imaginary time propagation with the inclusion of rotation ($\Omega \neq 0$) to observe the stationary vortex structures. When the condensate begins to rotate the multiply quantized vortices enter into the condensate from the surface. As time progress, these vortices approach to a stationary vortex configuration as shown in figure 5. We notice the basic configuration of centered single vortex surrounded by five
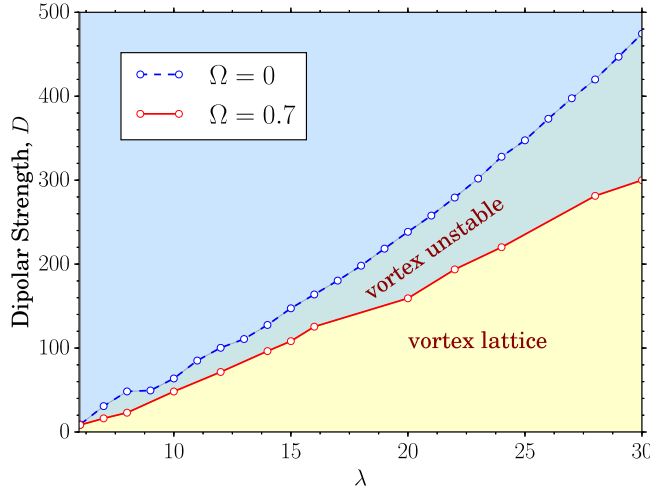
Figure 4. Stability diagram of a purely dipolar BEC in cylindrically symmetric trap as a function of trap aspect ratio (λ) and dipolar interaction parameter (D). Below the dotted blue line the local minimum with non-vortex state is stable while below the solid red line is the region of stable vortex lattice.

vortices at rotation frequency $\Omega = 0.7$ as shown in figure 5(b). At $\Omega = 0.8$ the vortex structure is shown in figure 5(c) resembles the structures observed in the references [16, 20] for dipolar condensates. Further, we observed the square lattice at $\Omega = 0.9$. To test the stability of the vortex structures, the relaxed solution is evolved in real -time for the same parameters of imaginary time. The vortex structure persisted as depicted in figure 6, even after long time evolution.

At high rotation frequency (e.g. $\Omega = 0.97$), we found 16 vortices as shown in figure 5(d). Moreover, one may note from figure 4 that, for obtaining the vortex lattice in the condensates with larger dipolar strength, it is necessary to consider significantly larger λ. In this case we choose the trap aspect ratio $\lambda = 30$ with dipolar interaction strength $D \simeq 300$ corresponding to about 118 000 ^{52}Cr atoms. We observed a similar arrangement in the vortex structures in $\lambda = 10$ and 30, when the number of vortices are equal. It tells us that the condensate tries to persist with the similar vortex structures, even though the trap aspect ratio or dipolar interaction strength are distinct. For instance, we noticed a qualitatively similar array of vortex lattices for both $\lambda = 10$ (see figure 6) and $\lambda = 30$ (see figure 7(b)), with $\Omega = 0.9$ and 0.3, respectively. We observe qualitatively similar structures for $\lambda = 10$ (see figure 5(d)) and $\lambda = 30$ (see figure 7(c)), with $\Omega = 0.97$ and 0.4, respectively. The condensate in a strong pancake trap creates a large number of vortices, even at low rotation frequency.
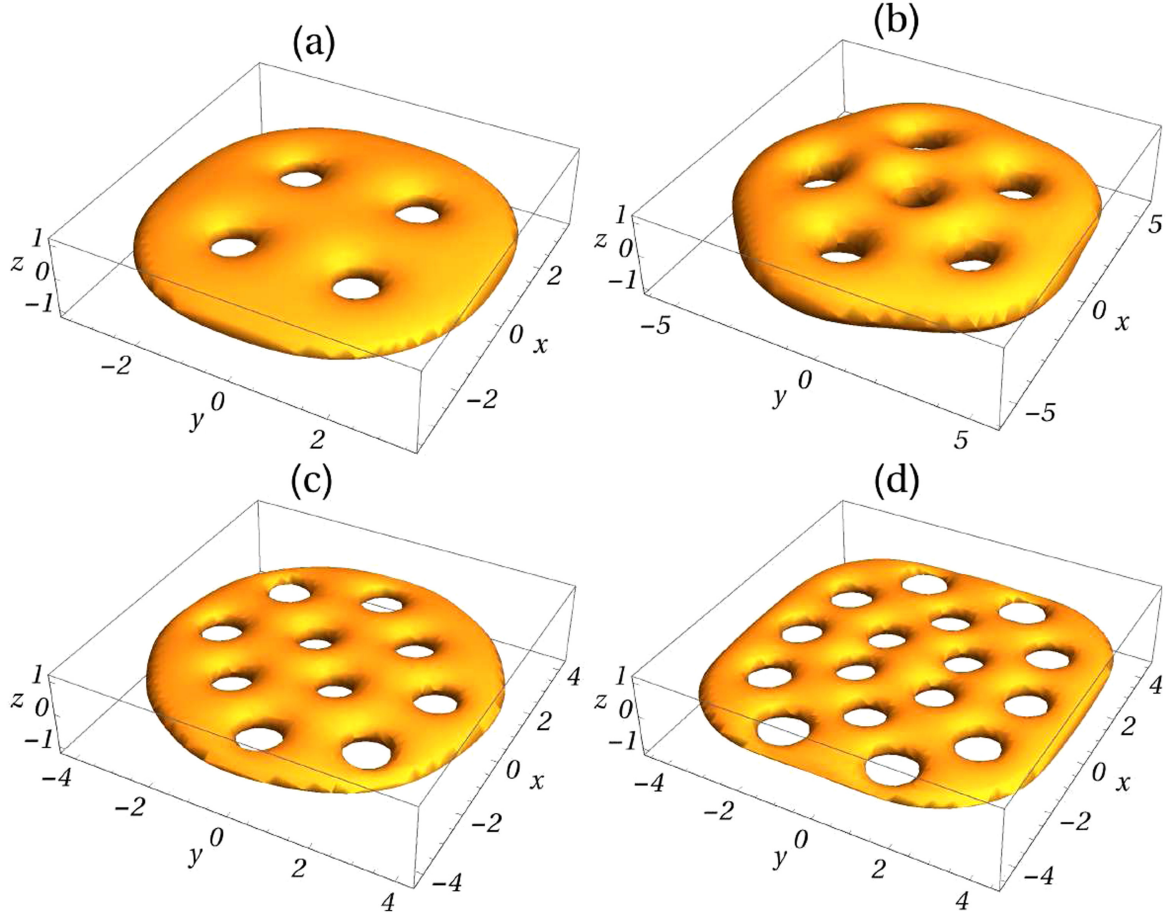
Figure 5. Three-dimensional view of condensate density $|\phi(x, y, z)|^2$ with vortex lattice of purely dipolar BECs with $a_{dd} = 16 \, a_0$, $a = 0$, $D = 38$, $\lambda = 10$ at rotation frequencies (a) $\Omega = 0.5$, (b) $\Omega = 0.7$, (c) $\Omega = 0.8$ and (d) $\Omega = 0.97$. The contour levels are taken as $|\phi(x, y, z)|^2 = 0.0125$.
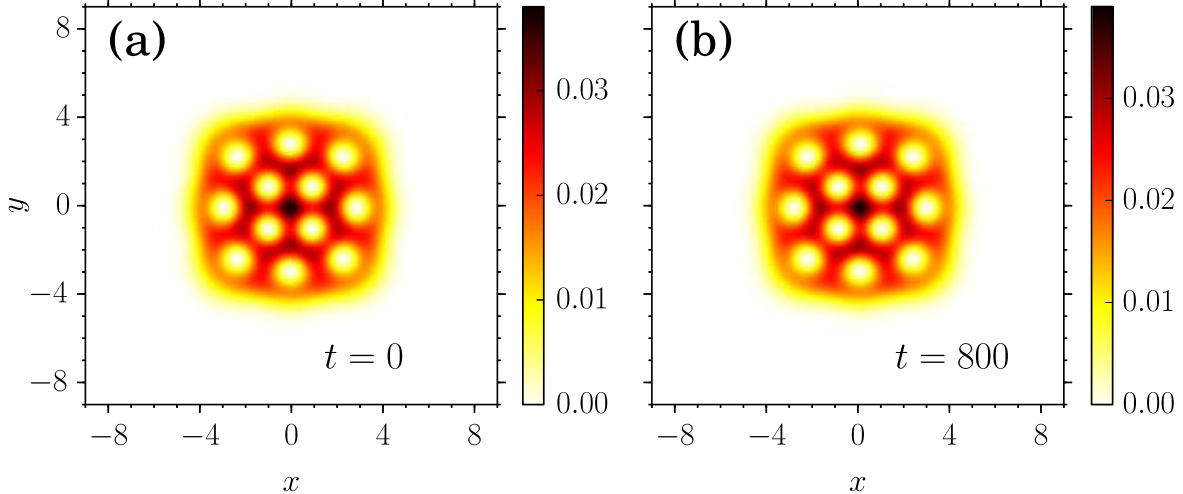
Figure 6. Two-dimensional view of the stable evolution of the condensate density $|\phi(x, y, 0)|^2$ with vortices arranged in a square lattice with $a_{dd} = 16\, a_0$, $a = 0$, $\lambda = 10$, $D = 38$, and $\Omega = 0.9$ at time, (a) $t = 0$ and (b) $t = 800$.

Further, we observed some distortion in the vortex lattice structure when the number of vortices is sufficiently large. In particular, the distortion is larger near to the surface than near to the center of the condensate. All the vortices have the same charge of vorticity, and their repulsion keeps the stable configuration. We note that the size of the vortex core radius becomes significantly larger in the vicinity of the surface than in the middle of the condensate while increasing the rotation frequency. Consequently, near to the surface, repulsive interaction diminishes the density of vortices and leads to the distortion in the vortex lattice. It is equivalent to observing transverse shear waves in quantum gases for large rotation frequencies [4]. In this regime, it takes place a decrease in the elastic shear strength of the vortex lattice.

In figures 8 and 9, we plot the calculated values of chemical potential, rms radius, and angular momentum as a function of rotation frequency for $\lambda = 10$ and 30. First, we calculate the chemical potential with respect to the rotation frequency in mean-field TF regime. When the interaction energy is large compared to the kinetic energy, the kinetic energy can be neglected and enters into TF regime. We assume the normalized density of the dipolar BEC of the form [34–37]

$$n(\mathbf{r}, t) \equiv |\phi(\mathbf{r}, t)|^2 = \frac{15}{8\pi R_\rho^2(t) R_z(t)}$$
$$\times \left[1 - \frac{\rho^2}{R_\rho^2(t)} - \frac{z^2}{R_z^2(t)}\right], \quad (5)$$

where $R_\rho(t)$ and $R_z(t)$ are the radial and axial sizes. In the TF regime one has the following set of coupled ordinary differential equations for the evolution of the condensate sizes [35]:

$$\ddot{R}_\rho = \frac{15N}{R_\rho R_z}\left[\frac{a}{R_\rho^2} - a_{dd}\left(\frac{1}{R_\rho^2} + \frac{3}{2}\frac{f(\bar{\kappa})}{R_\rho^2 - R_z^2}\right)\right] - R_\rho\gamma^2, \quad (6)$$

$$\ddot{R}_z = \frac{15N}{R_\rho^2}\left[\frac{a}{R_z^2} + 2a_{dd}\left(\frac{1}{R_z^2} + \frac{3}{2}\frac{f(\bar{\kappa})}{R_\rho^2 - R_z^2}\right)\right] - \lambda^2 R_z, \quad (7)$$

with $\kappa = R_\rho/R_z$, and

$$f(\kappa) = \frac{1 + 2\kappa^2 - 3\kappa^2 d(\kappa)}{1 - \kappa^2}, \quad d(\kappa) = \frac{\text{atanh}\sqrt{1 - \kappa^2}}{\sqrt{1 - \kappa^2}}. \quad (8)$$

Here the atomic scattering length is taken as $a = 0$ so that the dipolar interaction shows the dominant effect. It may be noted that the external rotation expands the condensate radially and shrinks it axially. As a consequence, the dependence of TF radii on Ω can be given by [2],

$$\frac{R_\rho(\Omega)}{R_\rho(0)} = (1 - \Omega^2)^{-3/10}, \quad \frac{R_z(\Omega)}{R_z(0)} = (1 - \Omega^2)^{1/5}. \quad (9)$$

Also, the chemical potential has the form

$$\mu_{TF}(\Omega) = \mu_{TF}(0)(1 - \Omega^2)^{2/5}. \quad (10)$$

As shown in figure 8(a) the chemical potential decreases continuously and it goes to zero when $\Omega = 1.0$. In figures 8(b)–(e) we plot the rms radius, $\sqrt{\langle r^2 \rangle} = \left(\int \phi^\star(\mathbf{r}, t)\, \mathbf{r}^2\, \phi(\mathbf{r}, t) d\mathbf{r}\right)^{1/2}$, and chemical potential as a function of rotation frequency calculated from the numerical solution of the GP equation. As expected, the condensate rms radius increases with the increase of rotation frequency due to the expansion of condensate. The rms radius is shown in figures 8(b) and (c) for $\lambda = 10$ and 30, respectively. One may note that, in the absence of rotation, the numerically calculated chemical potential compares well with TF results [31]. Whereas, in the presence of rotation, the TF chemical potential is about two times less than the numerically calculated value. In figures 8(d) and (e) we show the variation of chemical potential for $\lambda = 10$ and 30 respectively. Next, we calculate expectation value of angular momentum as a function of Ω from the numerical solution. Figure 9, depicts the plot of $\langle L_z \rangle$ with respect to Ω for $\lambda = 10$ and 30. The increase in the $\langle L_z \rangle$ is associated with the entry of vortices into the condensate. We are interested in studying the dependence of the vortex number (N_v) on the rotational frequency Ω in
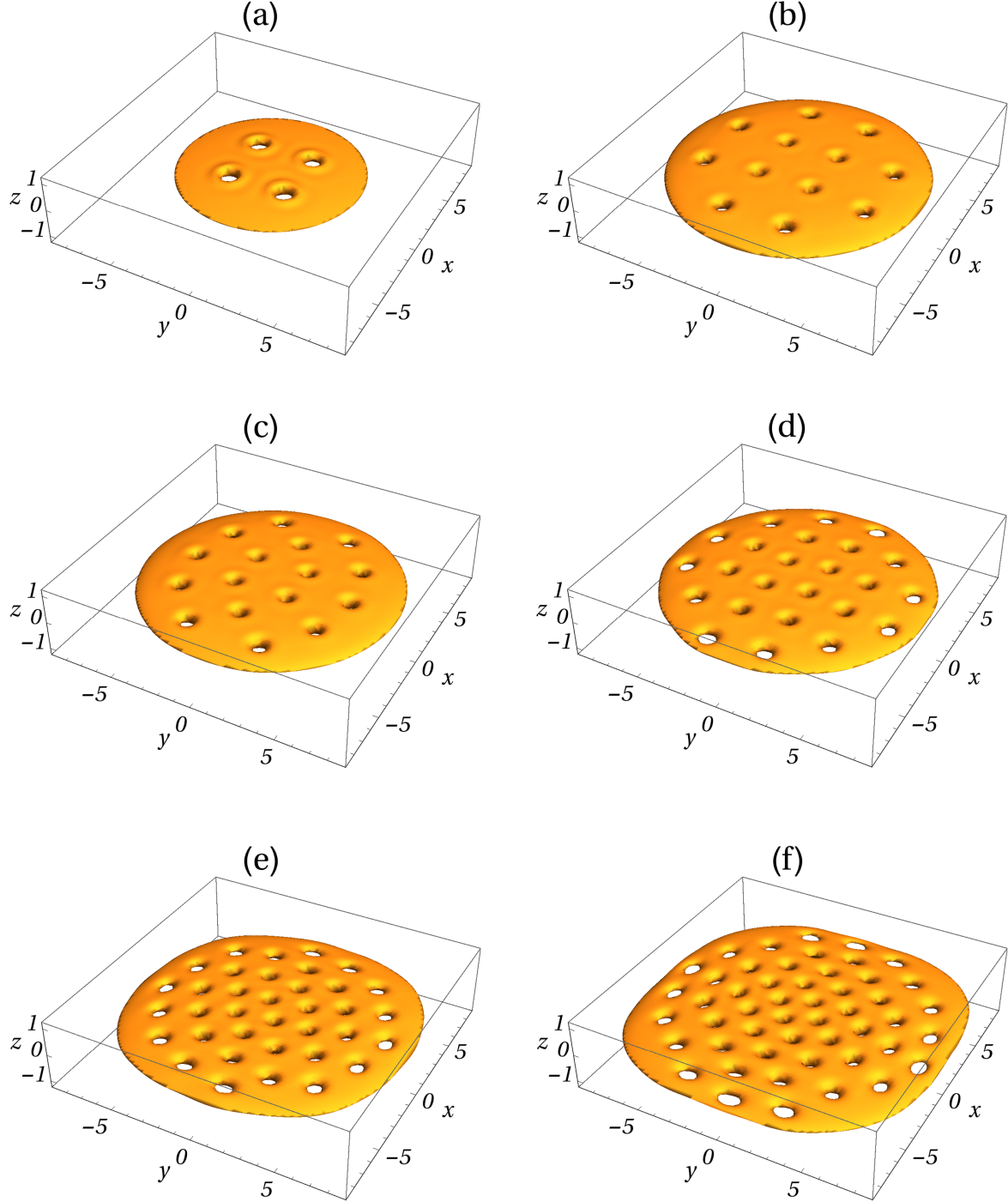
Figure 7. Three-dimensional view of condensate density $|\phi(x, y, z)|^2$ with vortex lattice of purely dipolar BECs with $a_{dd} = 16 \, a_0$, $a = 0$, $D = 300$, $\lambda = 30$ at rotation frequencies (a) $\Omega = 0.27$, $|\phi(x, y, z)|^2 = 0.0125$, (b) $\Omega = 0.3$, $|\phi(x, y, z)|^2 = 0.005$, (c) $\Omega = 0.4$, $|\phi(x, y, z)|^2 = 0.005$ and (d) $\Omega = 0.5$, $|\phi(x, y, z)|^2 = 0.005$ (e) $\Omega = 0.8$, $|\phi(x, y, z)|^2 = 0.005$, and (f) $\Omega = 0.97$, $|\phi(x, y, z)|^2 = 0.004$.

purely dipolar BEC. The rotating condensate has a dense array of vortices with a uniform density $n_v = m(\Omega\bar{\omega})/\pi\hbar$. The number of vortices present in the condensate is [2]

$$N_v = \frac{m(\Omega\bar{\omega})}{\hbar} R_\rho^2(\Omega). \tag{11}$$

The number of vortices increases linearly with Ω assuming the BEC in a fixed axially symmetric harmonic trap. The

radius $R_\rho(0)$ in TF regime can be calculated from the coupled equations (6) and (7), and the corresponding $R_\rho(\Omega)$ can be obtained from equation (9). In figure 10(a), we have estimated the number of vortices in the different harmonic trap aspect ratios $\lambda = 10, 20$ and 30 in TF regime and compared with numerically calculated equilibrium numbers. We noted some deviations in the number of vortices from TF results and calculated numerically. To compare the deviation in the
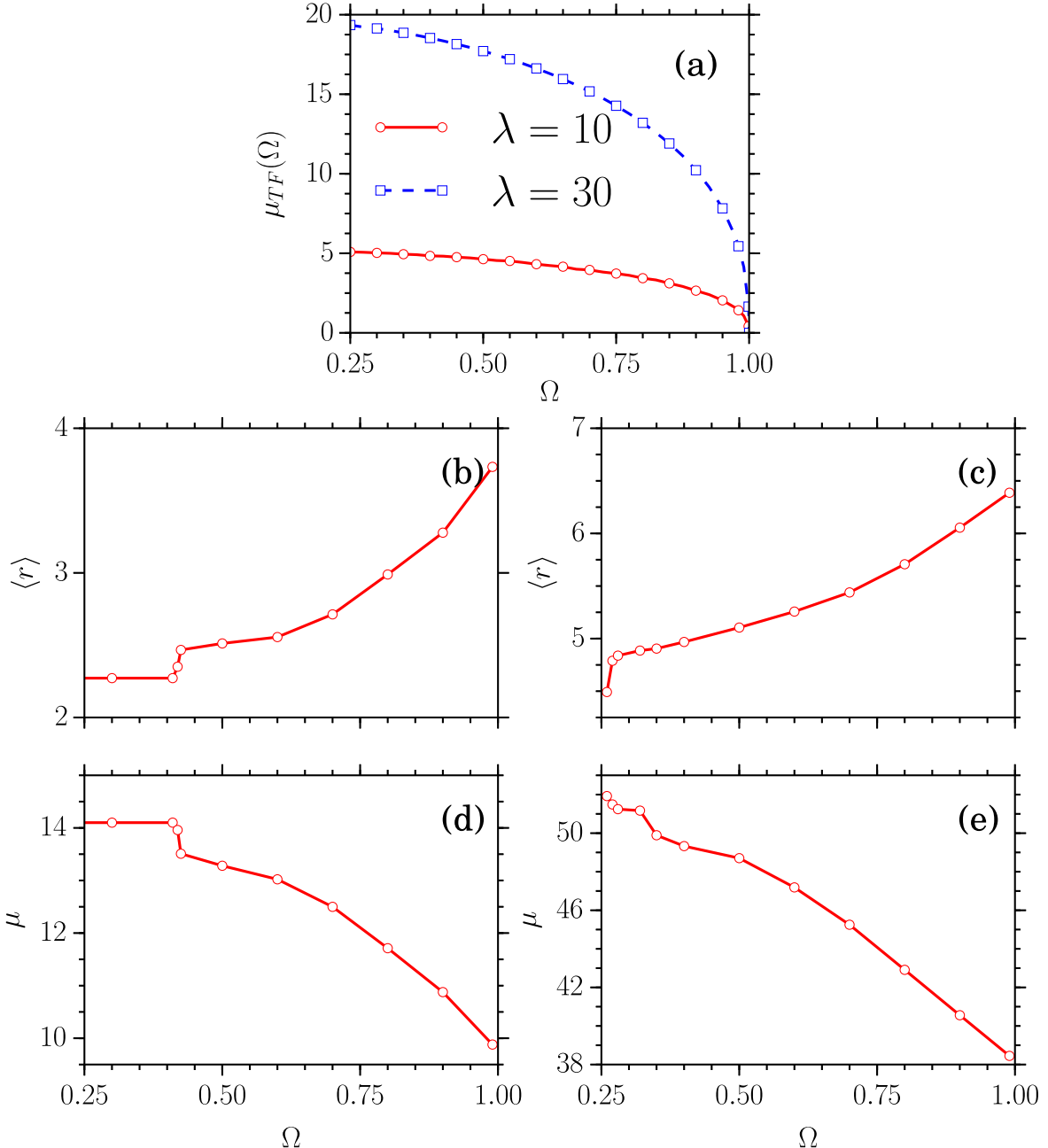
Figure 8. Plot of the chemical potential and rms radius as a function of the rotation frequency Ω for the dipolar BEC with the scattering length $a = 0$, λ=10 with $D \simeq 38$ and λ=30 with $D \simeq 300$. (a) TF chemical potential calculated from equation (10). Plot of the numerical calculation of radius and chemical potential in (b), (c) and (d), (e) respectively.

number of vortices in BEC without DDI, we calculate N_v for the BEC without DDI by tuning to the magic angle $\varphi = 54.7°$, where the dipolar interaction averages to zero in equation (4). Then we obtain N_v at $a = 50a_0$, $100a_0$ and we observe the deviation as shown in figure 10(b). In particular, when $\Omega > 0.9$ the deviation is larger and it is due to the strong expansion of condensate during the rapid rotation.

5. Vortex lattice in fully anisotropic trap

Finally, we concerned the purely dipolar BEC in fully anisotropic trap with $\gamma \neq \nu \neq \lambda$ in the equation (3). Whenever

$\gamma \neq \nu$, the system breaks the cylindrical symmetry. For the present analysis, we fix $\lambda = 10$, $\nu = 1$, and vary γ to study the changes in the spatial distribution of vortices in purely dipolar BECs by increasing the eccentricity of the trapping potential along x-direction. The condensate strongly elongates along the x-direction at $\gamma \leqslant 0.5$. The centrifugal force also elongates the condensate along x-direction. We have shown four linearly arranged vortices in figure 11(a) for $\gamma = 0.5$ and $\Omega = 0.425$. In figures 11 and 12, we observed linear and zig-zag arrangements of vortices with respect to the strength of eccentricity of the trap, respectively. Such linear and zig-zag vortex configurations have been observed in conventional
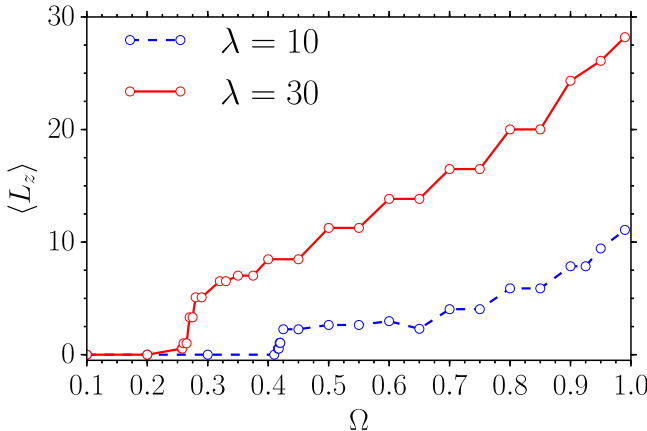
Figure 9. Plot of the expectation value of angular momentum $\langle L_z \rangle$ as a function of the rotation frequency Ω for the purely dipolar BEC trapped in $\lambda = 10, 30$ and $D \simeq 38, 300$, respectively.

quasi two-dimensional BEC [40]. Further increase in Ω splits the condensate at a critical rotation frequency (Ω_{sp}). In addition to the repulsive dipolar force between condensate atoms, the rotation provides supplementary elongation at $\Omega \geqslant \Omega_{sp}$. Splitting is a combined effect of rotation and dipolar forces. As rotation increases, the condensate creates extra vortices and also stretches. In the limiting case, it remains a vortex in the center and further stretching breaks the condensate in two parts. With further increase of rotation, no more vortices are generated since extra angular momentum can now be accommodated by orbital angular momentum. Stretching is enhanced depending on the trap geometries. We have observed only two vortices as shown in figure 12(a) at $\gamma = 0.7$ for the rotation frequency $\Omega = 0.425$. This is exactly half the number of vortices when compared to that with $\gamma = 0.5$ for the same rotation frequency. This evidences the dependence of the number of vortices on the eccentricity of the trap. At sufficiently high Ω_{sp}, the condensate splits into two parts as shown in figure 12(c). Here the splitting occurs at $\Omega_{sp} = 0.91$, which indicates that the trap with large γ requires substantially larger rotation frequency than the condensate with smaller γ. The phase of the vortices, marked with circles,

is shown in figures 11(d)–(f) and 12(d)–(f). We also marked few more vortices as red squares. These vortices are called hidden (or ghost) vortices since they cannot be observed in 3D density distribution. Due to hidden vortices, there is a phase defect distributed along the *y*-axis in the split condensate. A similar phase distribution is observed in rotating BEC in a double-well potential [38]. The splitting with vortices are also observed in normal BEC, where it is triggered by random noise or a complex frequency to the stationary vortices [39]. However, splitting is spontaneous in rotating dipolar BEC.

In figure 13, we show Ω_{sp} at different trap aspect ratios, $\lambda = 10, 30, 50$ and 100 with respect to the eccentricity of the trap γ. When the anisotropy is fixed as $\gamma = 0.5$ and $\lambda = 10$ then the splitting is observed at $\Omega_{sp} = 0.65$. One can observe that Ω_{sp} increases with increasing trap aspect ratio. For instance, when $\lambda = 50$ and 100 the corresponding required Ω_{sp} are 0.72 and 0.78, respectively. The strong axial trap preserves the condensate from splitting, and one needs to apply stronger Ω to observe it. On the other hand, if we increase the anisotropy to $\gamma = 0.7$, the Ω_{sp} also increases to 0.9 for $\lambda = 10$. The condensate does not split in strong enough axial traps as for $\gamma = 0.7$ and $\lambda = 50$ and 100. We have also carried out the calculations with an effective 2D GP equation in a rotating frame and observed a similar splitting with same vortex distribution for the corresponding parameters used in 3D calculations, confirming our results.

6. Summary and conclusion

In summary, we have studied the vortex lattice structures in purely dipolar BEC of ^{52}Cr atoms by considering the full three-dimensional GP equation. We have identified the stability regimes for non-vortex as well as vortex states in purely dipolar BECs with respect to both trap aspect ratio and DDI strength. The stability of vortex lattice structures are confirmed by real-time evolution. We have shown stationary vortex lattice structures for different trap aspect ratios within
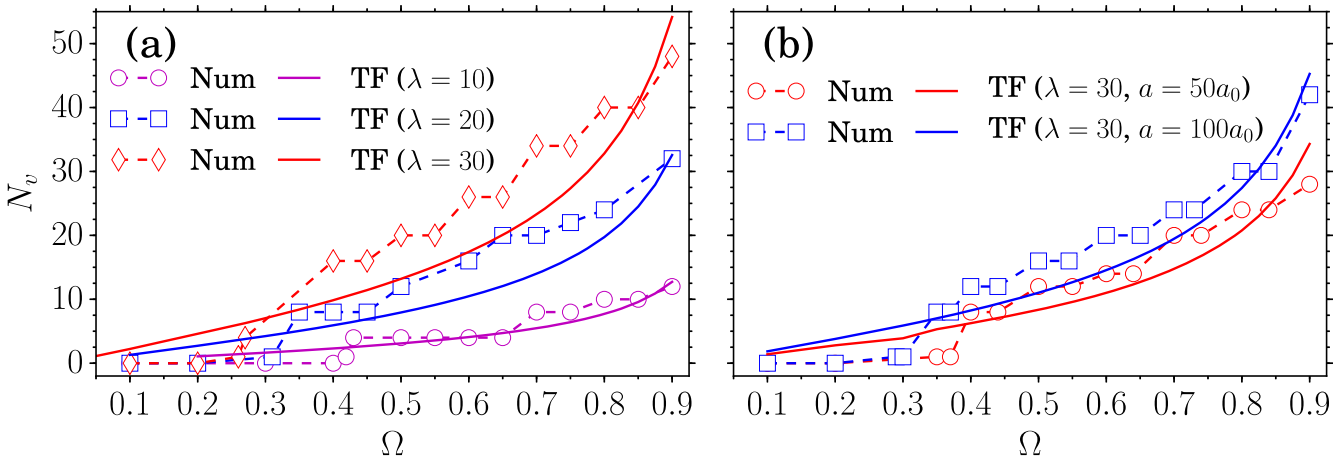
Figure 10. Plot of the equilibrium vortex number (N_v) as a function of the rotation frequency Ω for the (a) purely dipolar BEC trapped in $\lambda = 10, 20$ and 30, with $D = 38, 160$ and 300, respectively and (b) non-dipolar BEC trapped in $\lambda = 30$.
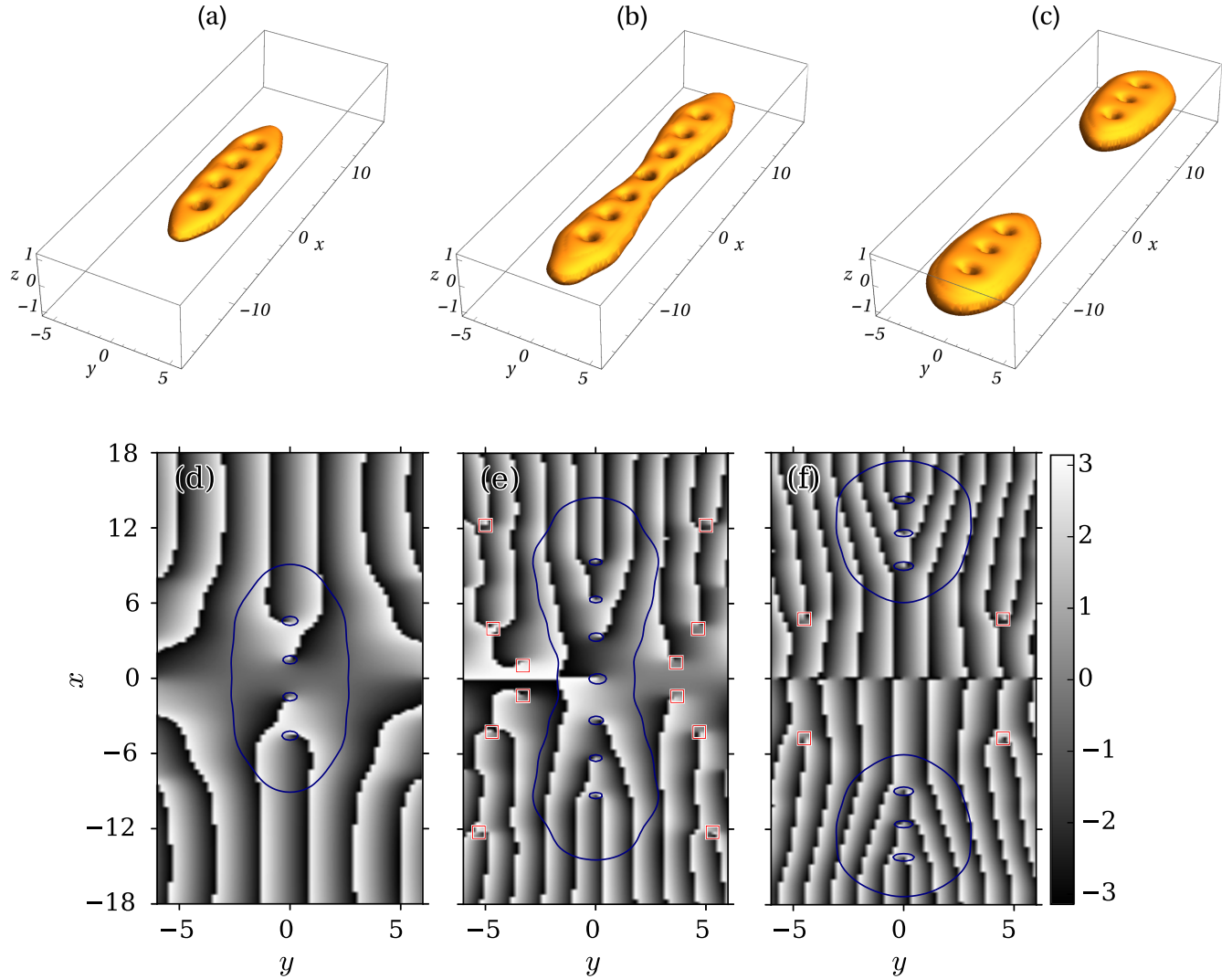
Figure 11. Vortex lattices in rotating dipolar BECs trapped in asymmetric trap with $\gamma = 0.5$, $\lambda = 10$, $D = 38$ and rotation frequency: (a) $\Omega = 0.425$, (b) $\Omega = 0.6$, (c) $\Omega = 0.7$. The contour levels are taken at $|\phi(x, y, z)|^2 = 0.01$, 0.005 and 0.002, respectively. The corresponding phase of the condensate density $|\phi(x, y, 0)|^2$ is shown in (d)–(f). Blue lines are density contour lines. Blue circles show the position of vortices, red squares show the center of hidden vortices.

the stability regime. Also, distortions in the lattices at high rotation frequencies have been observed.

We estimated the number of vortices using TF approximation and compared with those from numerical simulations. Further, we have analysed the spatial distribution of vortices in the fully anisotropic trap and observed linear and zig-zag arrangement of vortices. We noticed the breaking up of the condensates into two parts with an equal number of vortices. The splitting occurs due to a combination of centrifugal force due to rotation and repulsive dipolar interaction. Increasing rotation frequency creates extra vortices and stretches. Close to Ω_{sp} it appears a vortex at the center and further stretching breaks the condensate in two parts. Critical rotation frequency for splitting depends on the trap aspect ratio and dipolar parameters.

The predicted phase diagram of the stable vortex state will be useful to demonstrate the parameters such as dipolar strengths and trap aspect ratios for making experimental and

theoretical studies on rotating dipolar quantum gases. Further, the stability regime is relevant to investigate rapidly rotating dipolar BECs in the lowest Landau level. We found that dipolar BECs under rotation can produce square vortex lattices. This was found with two-component BECs [41] and recently in dipolar Fermi gas [42]. Observing the breaking in the rotating dipolar BECs in a fully anisotropic trap will be a new experimental exploration.

Acknowledgments
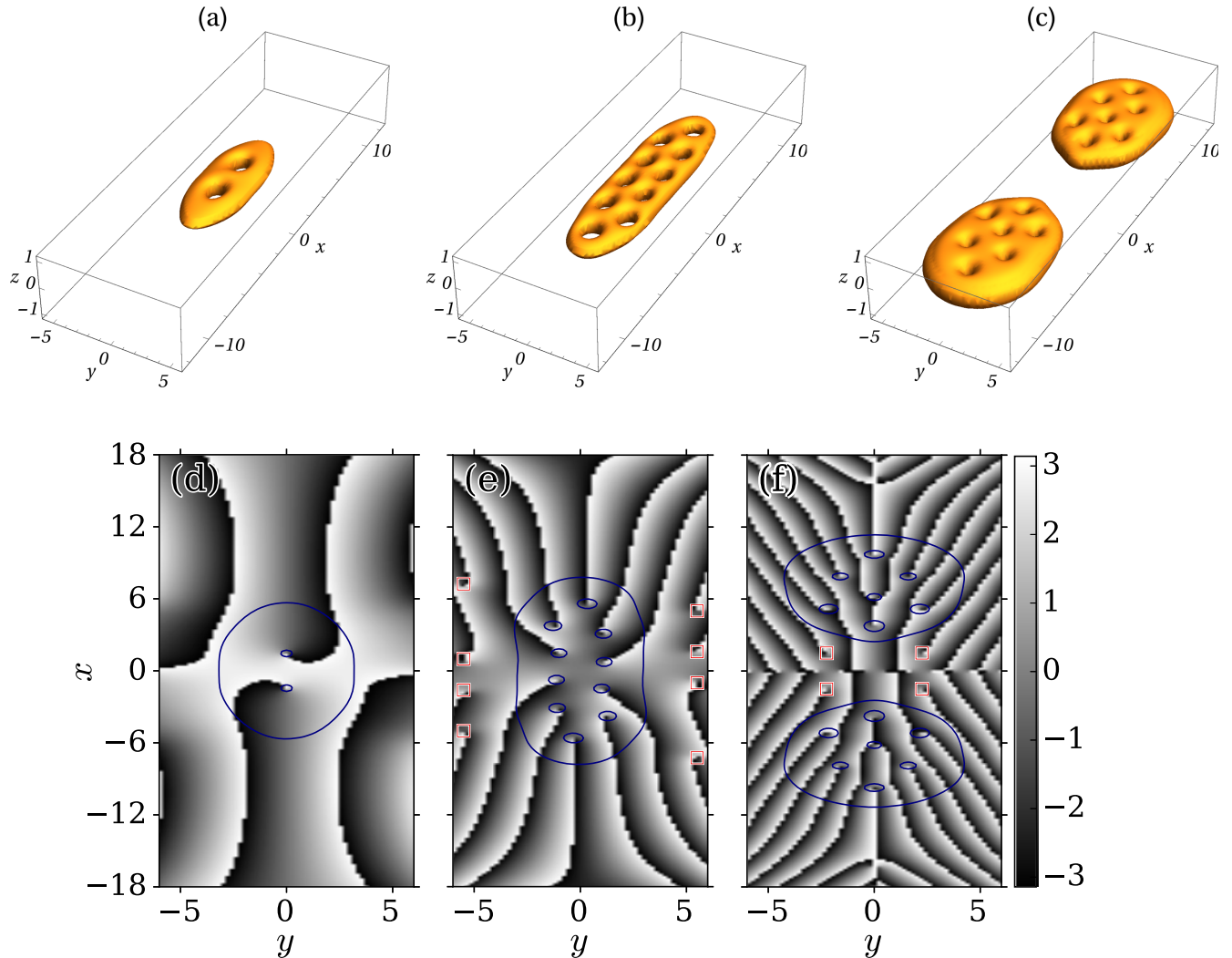
Figure 12. Vortex lattices in rotating dipolar BECs trapped in asymmetric trap with $\gamma = 0.7$, $\lambda = 10$, $D = 38$ and rotation frequency: (a) $\Omega = 0.425$, (b) $\Omega = 0.7$, (c) $\Omega = 0.91$. The contour levels are taken at $|\phi(x, y, z)|^2 = 0.02, 0.012$ and 0.002, respectively. The corresponding phase of the condensate density $|\phi(x, y, 0)|^2$ is shown in (d)–(f). Blue lines are density contour lines. Blue circles show the position of vortices, red squares show the center of hidden vortices.
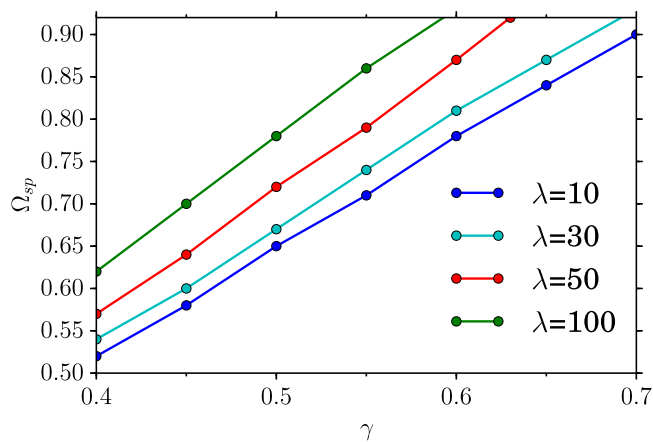
Figure 13. Critical rotation frequency (Ω_{sp}) for the splitting of the condensate with respect to anisotropy (γ) of the trap along x-direction for the parameters $\nu = 1$, $D = 38$ and for different trap aspect ratios $\lambda = 10, 30, 50$ and 100.

References

[1] Matthews M R, Anderson B P, Haljan P C, Hall D S, Wieman C E and Cornell E A 1999 *Phys. Rev. Lett.* **83** 2498
[2] Fetter A L and Svidzinsky A A 2001 *J. Phys.: Condens. Matter* **13** R135
Kevrekidis P G, Carretero-González R, Frantzeskakis D J and Kevrekidis I G 2004 *Mod. Phys. Lett.* B **18** 1481
Fetter A L 2009 *Rev. Mod. Phys.* **81** 647
Saarikoski H, Reimann S M, Harju A and Manninen M 2010 *Rev. Mod. Phys.* **82** 2785
[3] García-Ripoll J J and Pérez-García V M 2001 *Phys. Rev.* A **64** 053611
Aftalion A and Danaila I 2003 *Phys. Rev.* A **68** 023603

[4] Coddington I, Engels P, Schweikhard V and Cornell E A 2003 *Phys. Rev. Lett.* **91** 100402

[5] Minguzzi A, Succi S, Toschi F, Tosi M P and Vignolo P 2004 *Phys. Rep.* **395** 223

[6] Madison K W, Chevy F, Wohlleben W and Dalibard J 2000 *Phys. Rev. Lett.* **84** 806
Anderson B P, Haljan P C, Regal C A, Feder D L, Collins L A, Clark C W and Cornell E A 2001 *Phys. Rev. Lett.* **86** 2926
Leanhardt A E, Görlitz A, Chikkatur A P, Kielpinski D, Shin Y, Pritchard D E and Ketterle W 2002 *Phys. Rev. Lett.* **89** 190403
Henn E A L, Seman J A, Roati G, Magalhães K M F and Bagnato V S 2009 *Phys. Rev. Lett.* **103** 045301

[7] Dalibard J, Gerbier F, Juzeliūnas G and Öhberg P 2011 *Rev. Mod. Phys.* **83** 1523

[8] Aftalion A and Du Q 2001 *Phys. Rev. A* **64** 063603(R)
Baksmaty L O, Liu Y, Landman U, Bigelow N P and Pu H 2009 *Math. Comput. Simul.* **80** 131
Jeng B W, Wang Y S and Chien C S 2013 *Comp. Phys. Commun.* **184** 493

[9] Griesmaier A, Werner J, Hensler S, Stuhler J and Pfau T 2005 *Phys. Rev. Lett.* **94** 160401

[10] Lu M, Burdick N Q, Youn S H and Lev B L 2011 *Phys. Rev. Lett.* **107** 190401

[11] Aikawa K, Frisch A, Mark M, Baier S, Rietzler A, Grimm R and Ferlaino F 2012 *Phys. Rev. Lett.* **108** 210401

[12] Baranov M A 2008 *Phys. Rep.* **464** 71–111

[13] Lahaye T, Menotti C, Santos L, Lewenstein M and Pfau T 2009 *Rep. Prog. Phys.* **72** 126401

[14] Young-S L E and Adhikari S K 2012 *Phys. Rev. A* **86** 063611
Young-S L E and Adhikari S K 2013 *Phys. Rev. A* **87** 013618

[15] Andreev P A and Kuz'menkov L S 2014 *J. Phys. B: At. Mol. Opt. Phys.* **47** 225301

[16] Yi S and Pu H 2006 *Phys. Rev. A* **73** 061602(R)

[17] Wilson R M, Ronen S and Bohn J L 2009 *Phys. Rev. A* **79** 013621

[18] Abad M, Guilleumas M, Mayol R, Pi M and Jezek D M 2009 *Phys. Rev. A* **79** 063622
Abad M, Guilleumas M, Mayol R, Pi M and Jezek D M 2010 *Phys. Rev. A* **81** 043619

[19] van Bijnen R M W, O'Dell D H J, Parker N G and Martin A M 2007 *Phys. Rev. Lett.* **98** 150401

van Bijnen R M W, Dow A J, O'Dell D H J, Parker N G and Martin A M 2009 *Phys. Rev. A* **80** 033617

[20] Malet F, Kristensen T, Reimann S M and Kavoulakis G M 2011 *Phys. Rev. A* **83** 033628

[21] Kumar R K and Muruganandam P 2012 *J. Phys. B: At. Mol. Opt. Phys.* **45** 215301

[22] Kumar R K and Muruganandam P 2014 *Eur. Phys. J.* D **68** 289

[23] Ronen S, Bortolotti D C E and Bohn J L 2007 *Phys. Rev. Lett.* **98** 030406

[24] Dutta O and Meystre P 2007 *Phys. Rev. A* **75** 053604
Martin A D and Blakie B P 2012 *Phys. Rev. A* **86** 053623

[25] Bao W and Wang H 2006 *J. Comput. Phys.* **217** 612

[26] Giovanazzi S, Görlitz A and Pfau T 2002 *Phys. Rev. Lett.* **89** 130401

[27] Góral K and Santos L 2002 *Phys. Rev. A* **66** 023613

[28] Koch T, Lahaye T, Fröhlich, Griesmaier A and Pfau T 2008 *Nat. Phys.* **4** 218–22

[29] Brtka M, Gammal A and Tomio L 2006 *Phys. Lett. A* **359** 339

[30] Muruganandam P and Adhikari S K 2009 *Comp. Phys. Commun.* **180** 1888–912
Vudragović D, Vidanović I, Balaž A, Muruganandam P and Adhikari S K 2012 *Comp. Phys. Commun.* **183** 2021–5

[31] Kumar R K, Young-S L E, Vudragović D, Balaž A, Muruganandam P and Adhikari S K 2015 *Comp. Phys. Commun.* **195** 117–28

[32] Bao W, Cai Y and Wang H 2010 *J. Comput. Phys.* **229** 7874–92

[33] Carles R and Hajaiej H 2015 *Bull. London Math. Soc.* **47** 509–18

[34] Dalfovo F, Giorgini S, Pitaevskii L P and Stringari S 1999 *Rev. Mod. Phys.* **71** 463–512

[35] O'Dell D H J, Giovanazzi S and Eberlein C 2004 *Phys. Rev. Lett.* **92** 250401

[36] Eberlein C, Giovanazzi S and O'Dell D H J 2005 *Phys. Rev. A* **71** 033618

[37] Parker N G and O'Dell D H J 2008 *Phys. Rev. A* **78** 041601(R)

[38] Wen L, Xiong H and Wu B 2010 *Phys. Rev. A* **82** 053627

[39] Kuopanportti P and Möttönen M 2010 *Phys. Rev. A* **81** 033627

[40] Gullo N L, Busch T and Paternostro M 2011 *Phys. Rev. A* **83** 053612

[41] Liu C F, Fan H, Gou S C and Liu W M 2014 *Sci. Rep.* **4** 4224

[42] Ancilotto F 2015 *Phys. Rev. A* **92** 061602(R)